Volume 24
Number 9
7 March 2022
Pages 5249–5756

PCCP

Physical Chemistry Chemical Physics

rsc.li/pccp

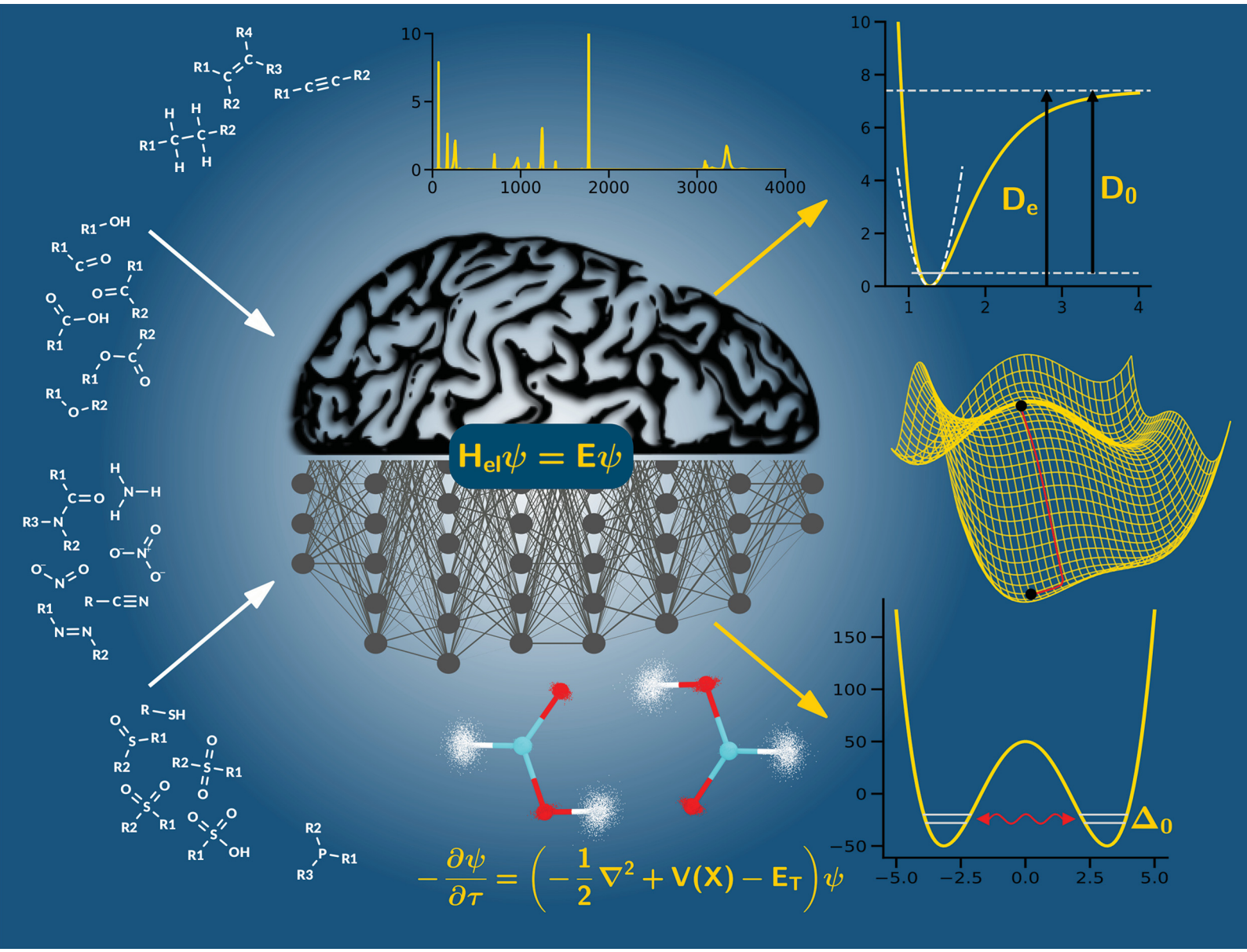

ISSN 1463-9076

ROYAL SOCIETY OF CHEMISTRY

PAPER

Silvan Käser and Markus Meuwly

Transfer learned potential energy surfaces: accurate anharmonic vibrational dynamics and dissociation energies for the formic acid monomer and dimer

PCCP

PAPER

View Article Online
View Journal | View Issue

Check for updates

Cite this: *Phys. Chem. Chem. Phys.*, 2022, **24**, 5269

Transfer learned potential energy surfaces: accurate anharmonic vibrational dynamics and dissociation energies for the formic acid monomer and dimer†

Silvan Käser and Markus Meuwly *

The vibrational dynamics of the formic acid monomer (FAM) and dimer (FAD) is investigated from machine-learned potential energy surfaces at the MP2 (PES_{MP2}) and transfer-learned (PES_{TL}) to the CCSD(T) levels of theory. The normal mode (MAEs of 17.6 and 25.1 cm^{-1}) and second order vibrational perturbation theory (VPT2, MAEs of 6.7 and 17.1 cm^{-1}) frequencies from PES_{TL} for all modes below 2000 cm^{-1} for FAM and FAD agree favourably with experiment. For the OH stretch mode the experimental frequencies are overestimated by more than 150 cm^{-1} for both FAM and FAD from normal mode calculations. Conversely, VPT2 calculations on PES_{TL} for FAM reproduce the experimental OH frequency to within 22 cm^{-1}. For FAD the VPT2 calculations find the high-frequency OH stretch at 3011 cm^{-1}, compared with an experimentally reported, broad ($\sim$100 cm^{-1}) absorption band with center frequency estimated at $\sim$3050 cm^{-1}. In agreement with earlier reports, MD simulations at higher temperature shift the position of the OH-stretch in FAM to the red, consistent with improved sampling of the anharmonic regions of the PES. However, for FAD the OH-stretch shifts to the blue and for temperatures higher than 1000 K the dimer partly or fully dissociates using PES_{TL}. Including zero-point energy corrections from diffusion Monte Carlo simulations for FAM and FAD and corrections due to basis set superposition and completeness errors yields a dissociation energy of D_0 = −14.23 ± 0.08 kcal mol^{-1} compared with an experimentally determined value of −14.22 ± 0.12 kcal mol^{-1}.

Received 24th September 2021,
Accepted 25th October 2021

DOI: 10.1039/d1cp04393e

rsc.li/pccp

Open Access Article. Published on 26 October 2021. Downloaded on 2/16/2026 3:25:57 PM.
This article is licensed under a Creative Commons Attribution-NonCommercial 3.0 Unported Licence.

1 Introduction

Vibrational spectroscopy is a powerful means to relate the structure and dynamics of molecules in the gas phase[1] and in solution.[2,3] Combined with state-of-the art atomistic simulation techniques, molecular-level information related to the structural dynamics of spectroscopic reporters (–CO, –NO, –SCN, $–N_3$),[4–8] or the thermodynamics in protein–ligand complexes[9,10] can be obtained. One of the pertinent questions is (a) whether or not classical molecular dynamics (MD) simulations can be used for accurate vibrational dynamics and (b) what level of theory and accuracy in representing the energies from electronic structure calculations is required for a meaningful contribution of simulations to assigning and interpreting experimentally determined spectra. Electronic structure calculations and their representations as full-dimensional potential energy surfaces (PESs) have progressed to a degree that now allows direct comparison with experiments.[11,12]

Generating full-dimensional, reactive PESs even for small molecules is a challenging task.[12,13] This often requires datasets consisting of tens of thousands of *ab initio* calculations to adequately describe configurational space of the system of interest. While calculations at the density functional theory (DFT) or Møller–Plesset perturbation (MP2) levels of theory are cost-efficient, reaction barriers are less accurate.[14] On the other hand, the "gold standard" coupled cluster with perturbative triples (CCSD(T)) approach scales as N^7 (with N being the number of basis functions)[15] which becomes quickly computationally prohibitive for full-dimensional PESs even for moderately sized molecules ($N_{atoms} \sim 10$). Recent applications of novel machine learning (ML) approaches combined with transfer learning (TL)[16–18] and related Δ-ML[19] in physical/computational chemistry[14,18,20–23] were shown to be data and cost-effective alternatives which will also be explored in the present work.

Formic acid (HCOOH), the simplest carboxylic acid, is an important intermediate in chemical synthesis and relevant to atmospheric chemistry.[24] It is also a promising fuel and H_2

Department of Chemistry, University of Basel, Klingelbergstrasse 80, CH-4056 Basel, Switzerland. E-mail: m.meuwly@unibas.ch

† Electronic supplementary information (ESI) available. See DOI: 10.1039/d1cp04393e

Open Access Article. Published on 26 October 2021. Downloaded on 2/16/2026 3:25:57 PM.
This article is licensed under a Creative Commons Attribution-NonCommercial 3.0 Unported Licence.

carrier[25,26] which can be produced by electrocatalytic CO_2 reduction reactions and, thus, may contribute to decreasing atmospheric CO_2 levels.[26,27] Formic acid monomer (FAM) and its dimer (formic acid dimer, FAD) have been the subject of several experimental[28–35] and theoretical[34,36–45] studies. In the vapor phase, formic acid exists as hydrogen bonded dimers[46] making it a prototype for complexes with hydrogen bonds such as enzymes or DNA base pairs.[47] The experimental IR spectrum has been reported for both, FAM and FAD.[28,30,34,48–53]

For FAM a recent study of both, *cis*- and *trans*-FAM, analyses a global PES constructed using regression techniques with energies from CCSD(T)(F12*)/cc-pVTZ-F12 calculations as the reference.[39] Vibrational eigenstates for both conformers were calculated using vibrational configuration interaction (VCI) and the fundamentals for *trans*-FAM were found to be in close agreement with experiment (RMSD = 3 cm^{-1}). Subsequently, a second full-dimensional CCSD(T)-F12a/aug-cc-pVTZ based PES for the two FAM conformers was used in multi-configuration time-dependent Hartree (MCTDH) vibrational calculations.[45] The *trans* fundamental transitions were found to agree to within 5 cm^{-1} with experiment. Additionally, vibrational states of deuterated *cis*- and *trans*-FAM were calculated using the block-improved relaxation method.[54] The two PESs[39,45] are further analyzed in detail in ref. 55 and are used for comparison with experiments for FAM and deuterated isotopologues of both isomers. Vibrational eigenstates were obtained from high order canonical Van Vleck perturbation theory (CVPT). Such high level anharmonic treatments of vibrations on high quality PESs are crucial for understanding and potentially (re)assigning experimental spectra as was found for *trans*-FAM:[39,45,55] assignment of the O–H in plane bend ν_5 which is in resonance with the O–H torsional overtone $2\nu_9$ has been ambiguous for a long time. Based on the high-level calculations the fundamental was assigned to 1306 cm^{-1} and the overtone to a spectroscopic feature at 1220 cm^{-1}. This assignment was subsequently supported by Raman jet experiment.[50] Interestingly, this reassignment was recently supported from second order vibrational perturbation theory (VPT2) calculations using a neural network-(NN) based PES.[23]

For FAD a considerable amount of computational work has been done on its dynamics,[56,57] infrared (IR) spectroscopy[34] and tunneling splittings.[40,41] A recent PES based on 13475 CCSD(T)-F12a energies with the cc-pVTZ and aug-cc-pVTZ basis sets for H and C/O atoms (CCSD(T)-F12a/haTZ), respectively, was fit to permutationally invariant polynomials[40] which reported a barrier for double proton transfer of 2853 cm^{-1} (8.16 kcal mol^{-1}). This was used for computing the zero-point energy (ZPE) based on diffusion Monte Carlo (DMC) calculations, for vibrational self consistent field (VSCF)/VCI calculations of fundamentals and to determine ground-state tunneling splittings in a reduced-dimensional approach. The tunneling splitting obtained was 0.037 cm^{-1} which is larger than the experimentally reported value[58,59] of 0.016 cm^{-1}. Subsequently,[41] the same PES was used for computing tunneling splittings without reducing the dimensionality of the problem using the ring-polymer instanton approach.[60] The value of 0.014 cm^{-1} was considerably closer to experiment and a more recent measurement based on IR techniques reported a tunneling splitting of 0.011 cm^{-1}.[61]

More recently the CCSD(T)-F12a PES was extended with a new dipole moment surface (DMS) at the MP2/haTZ level of theory and used for the analysis of the FAD IR spectrum.[42] Both, VSCF and VCI calculations were performed and compared with results from classical and "semi-classically" prepared quasi-classical MD simulations and experiment.[43] Classical MD corresponds to *NVE* simulations run at 300 K whereas the harmonic ZPE is added in the "semi-classically" prepared approach. For both approaches, the X–H stretch frequencies remain at higher frequencies compared to experiment. This effect is ascribed to the inability of MD simulations to correctly sample anharmonicities. The high-quality PES and DMS[42] were recently employed to assess the fingerprint region of FAD using variational vibrational computations and curvilinear kinetic energy operator representation.[62]

Experimentally, the dissociation energy of FAD into two FAMs has been determined from spectroscopy and statistical thermodynamics to be D_0 = 59.5(5) kJ mol^{-1} (~14.22 kcal mol^{-1}).[33] For the double proton transfer barrier, the most recent value from microwave spectroscopy (measured tunneling splitting of 331.2 MHz) is 2559 cm^{-1} (30.6 kJ mol^{-1} or 7.3 kcal mol^{-1}) from analysis of a 3D model.[63] This is consistent with a best value of 7.2 kcal mol^{-1} from a morphed MP2 surface that was determined from atomistic simulations and compared with IR experiments of the proton transfer band.[34] Earlier experiments reported a larger splitting of 0.0158 cm^{-1} (corresponding to 473.7 MHz) which yields a somewhat higher barrier for double proton transfer.[58] Yet more recent work in the infrared found 0.011367 cm^{-1} (340.8 MHz) which is closer to the most recent microwave data.[61]

In order to assess the expected magnitude of error cancellation due to shortcomings in the electronic structure method used and the fact that MD-based spectroscopy only samples the bottom of the potential well at ambient conditions, extensive higher-level calculations at the MP2 and CCSD(T) levels of theory were carried out together with the aug-cc-pVTZ basis set. This reference data was then represented as a NN based on the PhysNet architecture.[64] Additionally, TL[16–18] to the CCSD(T)/aug-cc-pVTZ level of theory was used to further improve the quality of the PES. Using these PESs for formic acid monomer and dimer, the harmonic and anharmonic vibrations, and the IR spectrum from finite-temperature MD simulations are determined. From this the complexation-induced red shifts can be determined and compared with experiment. Furthermore, DMC simulations are run to obtain an estimate for the ZPE of both molecules. The DMC calculations are a meaningful probe for the robustness of the PES and the resulting ZPEs are used for the determination of the binding energy of the dimer.

First, the methods are presented and discussed. Next, the accuracy of the NN-based PESs is assessed and the vibrational spectra for FAM and FAD are determined and compared with experiment. Then, the results from DMC simulations are presented and, finally, the results are discussed and conclusions are drawn.

 This journal is © the Owner Societies 2022

Open Access Article. Published on 26 October 2021. Downloaded on 2/16/2026 3:25:57 PM.
This article is licensed under a Creative Commons Attribution-NonCommercial 3.0 Unported Licence.

2 Computational details

2.1 Electronic structure calculations and PhysNet representation

The PESs for FAM and FAD are represented by a NN of the PhysNet architecture,[64] which has been used for different chemical systems recently.[20,21,65–68] PhysNet is a high-dimensional NN[69] of the "message-passing" type.[70] It constructs a feature vector for each atom in a molecule describing the atom's local chemical environment. These feature vectors (descriptors) are iteratively refined (learned) and used to predict atomic contributions to the total energy E and partial charges q_i. The forces $\boldsymbol{F}_i$ needed to run MD simulations are obtained from reverse-mode automatic differentiation[71] and the molecular dipole moment is calculated from the partial charges following $\boldsymbol{\mu} = \sum_i q_i \boldsymbol{r}_i$. Details of the PhysNet approach are described elsewhere.[64] The parameters of PhysNet are fitted to *ab initio* energies, forces and dipole moments calculated at the MP2[72]/aug-cc-pVTZ[73] level of theory using Molpro.[74]

A dataset of reference structures is required for training PhysNet. An ensemble of 20 000 FAM (5000) and FAD (15 000) geometries are generated from Langevin dynamics at 2000 K using the atomic simulation environment (ASE)[75] at the PM7 level of theory.[76,77] For FAD, the transition state (TS) region is sampled by harmonically biasing the geometry toward the TS structure, similar to the umbrella sampling approach.[78] This dataset is extended with geometries of fragments of the FAM molecule (H_2, CH_4, H_2O, CO, H_3COH, H_2CO) following the amons approach.[79] For the amons, 1000 geometries each are generated using Langevin dynamics at 1000 K. Based on initial PhysNet representations of the PES, the dataset was extended with one round of adaptive sampling.[80,81] The final MP2 dataset contains 26 000 reference structures and was split randomly according to 20 800/2600/2600 for training/validation/testing. Henceforth, this PES is referred to as PES_{MP2}.

To further improve the quality of the PES, TL[16–18] from the MP2 to the CCSD(T) level of theory was performed. The data set for TL contained 866 geometries: 425 for FAM and 441 for FAD. For FAM, they were generated from normal mode sampling[82] at different temperatures (between 10 and 2000 K) and geometries for FAD were those along the minimum energy path (MEP), along particular normal modes and geometries obtained from normal mode sampling. *Ab initio* energies, forces and dipole moments for the 866 geometries were determined at the CCSD(T)/aug-cc-pVTZ[73,83,84] level of theory using MOLPRO.[74] Then, the PhysNet model was retrained on the TL-data set by initializing the NN with the parameters from the trained NN at the MP2 level as a good initial guess. The data set was split randomly according to 85/10/5% into training/validation/test set and the learning rate was reduced to 10^{-4} compared with 10^{-3} when learning a model from scratch. The final TL PES is referred to as PES_{TL}.

2.2 Vibrational calculations

Harmonic and anharmonic frequencies can be determined using PES_{MP2} and PES_{TL}. First, harmonic frequencies are computed from diagonalization of the mass-weighted Hessian matrix. Next, anharmonic frequencies are obtained (i) from finite-temperature IR spectra calculated from the dipole–dipole autocorrelation function[85–87] of MD simulations and (ii) from VPT2 as implemented in the Gaussian software[88] using PES_{MP2} and PES_{TL} as external potentials.

Finite-temperature MD simulations were carried out using ASE[75] and PES_{MP2} and PES_{TL}. The trajectories are started from the equilibrium geometry of FAM and FAD, respectively, and initialized with random momenta drawn from a Maxwell–Boltzmann distribution corresponding to 300 K and the simulations are carried out in the *NVE* ensemble with a time step of Δt = 0.5 fs. After equilibration for 50 ps the simulations are propagated for 200 ps. The molecular dipole moment $\mu(t)$ is recorded for structures separated by 0.5 fs and the dipole–dipole autocorrelation is computed as $C(t) = \langle \mu(0)\mu(t) \rangle$. Infrared spectra $C(\omega)$ are then obtained by Fourier transformation of $C(t)$ and applying a Blackman filter. All finite-temperature spectra are averages over 1000 independent *NVE* MD simulations.

2.3 Diffusion Monte Carlo

DMC calculations are used to determine ZPEs (*i.e.* the quantum ground state energy) for FAM and FAD, and to examine PES_{TL} for holes. Here, the unbiased DMC algorithm was used.[14,89,90] A set of thousands to tens of thousands of random walkers is initialized and subsequently the atoms in each walker are displaced randomly at every timestep. The ensemble of walkers represents the nuclear wavefunction of the molecule. Based on a walker's potential energy E_i with respect to a reference energy, E_r, they remain alive and can give birth to new walkers, or can be killed. The walkers die and replicate according to the following probabilities:[14]

$$P_{\text{death}} = 1 - e^{-(E_i - E_r)\Delta\tau} \quad (E_i > E_r) \tag{1}$$

$$P_{\text{birth}} = e^{-(E_i - E_r)\Delta\tau} - 1 \quad (E_i < E_r). \tag{2}$$

Here, $\Delta\tau$ is the step size in imaginary time. Following each time step, the dead walkers are removed and E_r is updated according to

$$E_r(\tau) = \langle V(\tau) \rangle - \alpha \frac{N(\tau) - N(0)}{N(0)} \tag{3}$$

In eqn (3) $\langle V(\tau) \rangle$ is the averaged potential energy over the alive walkers, α is the magnitude of fluctuations in the number of walkers and is a parameter, and $N(0)$ and $N(\tau)$ are the number of alive walkers at times 0 and τ, respectively. The ZPE is then approximated as the average of E_r over all imaginary times.

Following ref. 14, the DMC calculations were performed in Cartesian coordinates and in full dimensionality. For both, FAM and FAD, ten independent DMC simulations were performed. To obtain an estimate of the ZPEs 30 000 walkers were advanced for 50 000 time steps following an equilibration period of 5000 time steps. A step size of $\Delta\tau$ = 5.0 a.u. was used. For converging the DMC simulations outlined above and to obtain statistically meaningful results more than 3×10^{10}(= 30 000 × 55 000 × 10 × 2) energy evaluations were required in total.

Open Access Article. Published on 26 October 2021. Downloaded on 2/16/2026 3:25:57 PM.
This article is licensed under a Creative Commons Attribution-NonCommercial 3.0 Unported Licence.

The computational efficiency of a PES is crucial for DMC simulations which requires a large number of energy evaluations. The Tensorflow library,[91] in which PhysNet is implemented, allows training and evaluation of the NN on graphics processing units (GPUs). The use of GPUs for the evaluation of PhysNet speeds up the calculations as they can be performed in a highly parallel manner.[92] Here, all DMC calculations were performed on a GeForce RTX 2080Ti GPU with 12 Gb of RAM. Each DMC simulation for FAM (FAD) takes 8.7 (23.7) h on average.

3 Results

3.1 Quality of the PhysNet PES_{MP2} and PES_{TL}

First, the quality of the NN-learned energy functions is considered. To assess the reproducibility of the PhysNet models, two independent models are trained for the MP2 reference data. Both are evaluated on a test set containing 2600 randomly chosen structures of the dataset which were not used during training. The model yielding lower mean absolute and root mean squared errors (MAE and RMSE) on the test set is then used for the simulations and for TL. The out of sample performances of both PES_{MP2} and PES_{TL} are summarized in Table 1 and Fig. 1.

The better of the two PES_{MP2} is characterized by MAE(E) = 0.012 kcal mol^{-1}, RMSE(E) = 0.019 kcal mol^{-1}, MAE(F) = 0.026 kcal mol^{-1} Å^{-1} and RMSE(F) = 0.195 kcal mol^{-1} Å^{-1}. Accuracies similar to PES_{MP2} are achieved for PES_{TL}, although the test set (44 geometries) is smaller than for learning at the MP2 level: the performance is MAE(E) = 0.007 kcal mol^{-1}, RMSE(E) = 0.016 kcal mol^{-1}, MAE(F) = 0.076 kcal mol^{-1} Å^{-1}, and RMSE(F) = 0.580 kcal mol^{-1} Å^{-1}, see Table 1 which also reports results for the dipole moments.

The quality of PES_{MP2} can also be assessed in terms of molecular geometries and the energy barrier for double proton transfer. The MP2/AVTZ optimized geometries of FAM, FAD and the proton transfer TS (see Tables S1–S3, ESI†) are reproduced by PES_{MP2} with RMSEs smaller than 0.003 Å. The energy barrier for PES_{MP2} is 6.69 kcal mol^{-1} compared with 6.71 kcal mol^{-1} from *ab initio* calculations, *i.e.* a difference of 0.02 kcal mol^{-1}. The proton transfer barrier, which is underestimated at the MP2 level of theory, is one of the essential features of the FAD PES_{TL}. Earlier studies at the coupled cluster level of theory yielded barrier heights of 7.95, 8.16 and 8.30 kcal mol^{-1} using the CCSD(T)-F12a/haDZ, CCSD(T)-F12a/haTZ//CCSD(T)-F12a/haDZ and CCSD(T)/aV5Z//MP2/aV5Z level of theory, respectively.[37,40] The barrier for DPT at the CCSD(T)/aug-cc-pVTZ level was found to be 7.9 kcal mol^{-1}.[34] This agrees favourably with a barrier of 7.92 kcal mol^{-1} from the present PES_{TL}. The experimental barrier height is estimated to be 7.3 kcal mol^{-1} using a 3D-model to reproduce the tunneling splitting of 331.2 MHz.[63] A somewhat lower barrier for DPT (7.2 kcal mol^{-1}) was also found from morphing an MP2-based full-dimensional PES to reproduce the experimentally observed, broad IR absorption from finite-temperature MD simulations.[34]

The dissociation energy D_e on PES_{TL} for FAD into two FAMs is −16.79 kcal mol^{-1} which is identical to that from explicit *ab initio* calculations at the CCSD(T)/AVTZ level of theory.[38] Because the training set for the full-dimensional PES contains structures of FAM and FAD, dissociation along the reaction path connects the minimum energy structures of the two asymptotic states (2 separate FAMs and FAD, respectively).

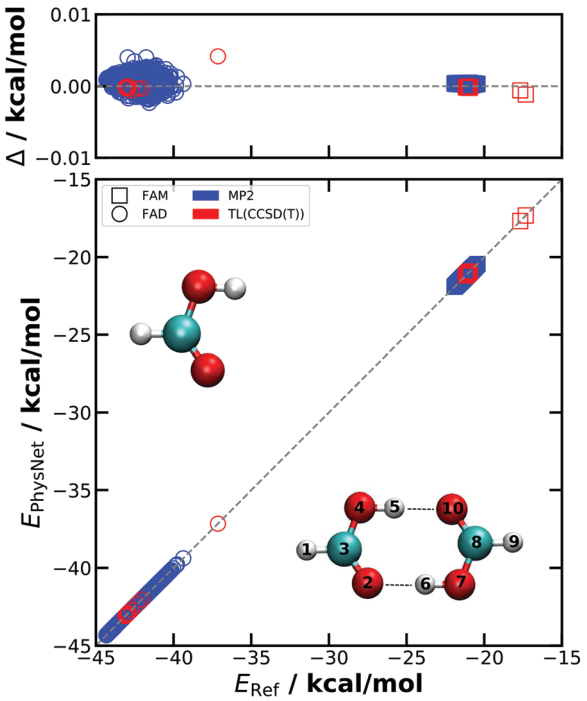

Fig. 1 The accuracy of the PES_{MP2} and PES_{TL} energies is shown with respect to the appropriate reference *ab initio* values taken from the separate test sets. For PES_{MP2}, only the performance of the superior model is shown and only FAM and FAD geometries of the test set are considered. The deviations $\Delta = E_{Ref} - E_{PhysNet}$ for geometries in the test sets remain well below 0.01 kcal mol^{-1}. The structures of FAM and FAD are shown together with labels and the hydrogen bonds indicated by dotted lines.

Table 1 Out of sample errors for two MP2 and the TL models. Both $PESs_{MP2}$ are evaluated on a test set containing 2600 randomly chosen structures of the dataset which were not used during training. $PES1_{MP2}$ is chosen for further analysis due to better overall performance. PES_{TL} is tested on a separate test set containing 44 geometries. The energy, force and dipole moment errors are given in kcal mol^{-1}, kcal mol^{-1} Å^{-1} and Debye, respectively. Additionally, the R^2 coefficient for the energy is shown

	$PES1_{MP2}$	$PES2_{MP2}$	PES_{TL}
MAE(E)	0.012	0.014	0.007
RMSE(E)	0.019	0.028	0.016
MAE(F)	0.026	0.029	0.076
RMSE(F)	0.195	0.411	0.580
MAE(μ)	0.001	0.001	0.002
RMSE(μ)	0.002	0.002	0.008
$1 - R^2(E)$	3.7×10^{-9}	8.5×10^{-9}	4.1×10^{-9}

3.2 Harmonic frequencies

The FAM harmonic frequencies calculated from the two PhysNet PESs are compared to their respective MP2 and CCSD(T) reference values in Fig. 2 (squares) and Table S4 (ESI†) reports all frequencies. The harmonic frequencies on PES_{MP2} reproduce

This journal is © the Owner Societies 2022

Open Access Article. Published on 26 October 2021. Downloaded on 2/16/2026 3:25:57 PM.
This article is licensed under a Creative Commons Attribution-NonCommercial 3.0 Unported Licence.

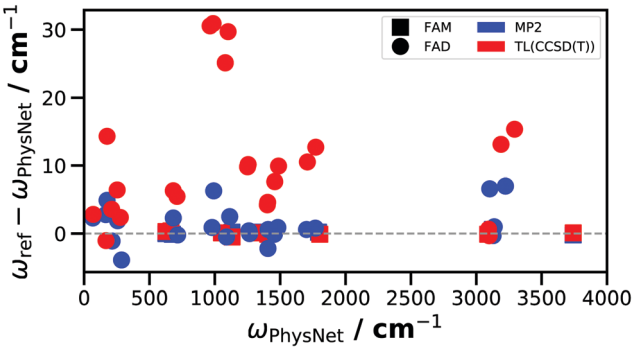

Fig. 2 The accuracy of harmonic frequencies using PES_{MP2} and PES_{TL} compared with the corresponding reference *ab initio* values. The FAD CCSD(T) values are taken from ref. 36. Almost no error is visible for FAM whereas errors up to ~30 cm^{-1} are found for FAD.

their reference frequencies with a MAE of 0.2 cm^{-1}. It is noteworthy that PES_{TL} is able to reproduce the CCSD(T) harmonic frequencies of FAM with a MAE of 0.2 cm^{-1} with only 425 FAM geometries used in the TL.

Similarly for FAD, the PhysNet harmonic frequencies are compared with those from direct *ab initio* calculations in Fig. 2 (circles) and Table S5 (ESI†). Frequencies from PES_{MP2} match the *ab initio* harmonic frequencies with a MAE of 2.1 cm^{-1} and a maximum unsigned deviation of 7 cm^{-1} for mode 24. For FAD the harmonic frequencies on PES_{TL} show a somewhat larger MAE than frequencies from PES_{MP2}. The reference CCSD(T)/aug-cc-pVTZ harmonic frequencies were those from ref. 36. The MAE between reference frequencies and those from PES_{TL} is 10.7 cm^{-1} and deviations up to ~30 cm^{-1} for single frequencies occur.

3.3 VPT2 calculations

VPT2 calculations are carried out for FAM and FAD using PES_{MP2} and PES_{TL} as a complement to finite-*T* spectra, see Fig. 3 and 4 and Table 2. The VPT2 frequencies for FAM obtained from PES_{TL} agree well with experiment (MAE of 8.4 cm^{-1}) for which the largest deviation is found for the highest frequency mode, *i.e.* a difference of 22.2 cm^{-1}. The corresponding intensities capture the general trend of the experiment and, converse to the finite-*T* spectra (see below), even the intensities of the two lowest modes agree with experiment (see Fig. 3). For FAD, the MAE of the VPT2 frequencies is 19.3 cm^{-1} compared with experiment whereas the intensities agree favourably (see Fig. 4). For FAD the MAEs of the VPT2 calculations on the two NN-learned PESs with respect to MP2 reference and experiment are 6.4 cm^{-1} (PES_{MP2}) and 19.3 cm^{-1} (PES_{TL}), respectively. For PES_{TL} the deviations are largest for the low (modes 1 to 6, MAE of 30.2 cm^{-1}) and high frequency vibrations (modes 22 to 24), see Table 2.

One interesting observation concerns the correct assignment[55] of the fundamental ν_5 (mode 5 in Table 2) and $2\nu_9$ (first overtone of mode 2 in Table 2) modes in FAM. VPT2 calculations using PES_{TL} find ν_5 at 1296.0 cm^{-1} and $2\nu_9$ = 1211.9 cm^{-1} which is consistent with recent Raman data measured in a jet reporting a frequency of 1306 cm^{-1} and 1220 cm^{-1} for the fundamental and

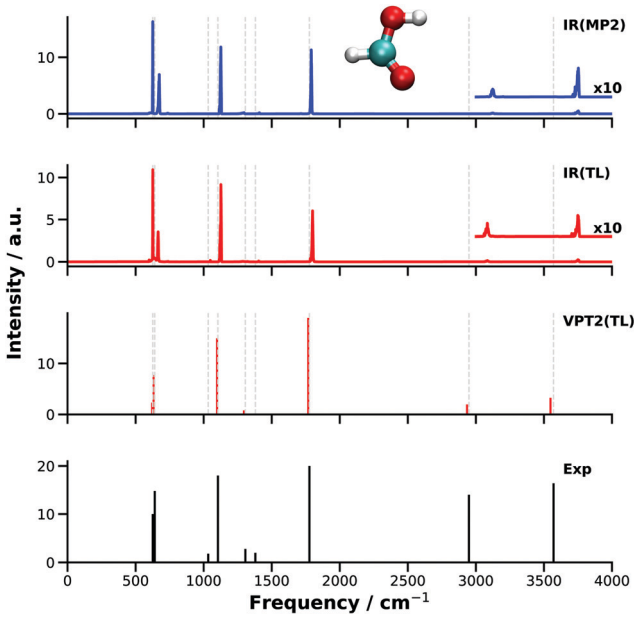

Fig. 3 Infrared spectrum of FAM obtained from PES_{MP2} (blue) and from PES_{TL} (red) using finite-*T* simulations (IR) and the VPT2 approach. The results are complemented with experimental frequencies for comparison.[29,39] The gray dashed lines indicate the positions of the experimental frequencies and the XH peaks are scaled for better readability. The intensities of the VPT2 calculation capture the general trend of the experimental measurements whereas it is less clear for the finite-*T* spectra. The finite-*T* spectra (IR) are calculated from the dipole–dipole auto-correlation function of 1000 MDs each run for 200 ps with PES_{MP2} and PES_{TL} at 300 K.

the overtone, respectively.[50] VPT2 calculations at the MP2 level using PES_{MP2}, on the other hand, find ν_5 = 1220.6 and $2\nu_9$ = 1297.9 cm^{-1}, *i.e.* the opposite assignment compared with experiment and calculations at the higher level of theory.

For the errors of the VPT2 calculation of FAD there are several potential reasons. First, PES_{TL} is less accurate in reproducing harmonic frequencies at the CCSD(T) level. Secondly, the low frequency harmonic modes 1 to 6 agree well with experiment (see Table S5, ESI†). However, VPT2 determines anharmonic corrections to be added to or subtracted from the harmonic frequencies. Hence, if the harmonic frequencies agree well with experiment, the VPT2 frequencies potentially differ from experimental values and the disagreement is larger for larger anharmonic corrections as is often the case for low frequency vibrations. Thirdly, VPT2 calculations also may incur larger errors, in particular for proton-bound dimers with large amplitude motions.[98] Finally, the above errors can also accumulate which then leads to worse agreement between experimentally observed and computed anharmonic frequencies despite the high quality of PES_{TL}. It should be noted that VPT2 calculations at the CCSD(T) level using conventional electronic structure codes for FAM is computationally demanding and for FAD it is unfeasible. To this end, more approximate, hybrid schemes using harmonic frequencies from a higher calculation (*e.g.* CCSD(T)) and anharmonic corrections calculated at a lower level of theory (*e.g.* MP2) were applied for FAD.[38]

Open Access Article. Published on 26 October 2021. Downloaded on 2/16/2026 3:25:57 PM.
This article is licensed under a Creative Commons Attribution-NonCommercial 3.0 Unported Licence.

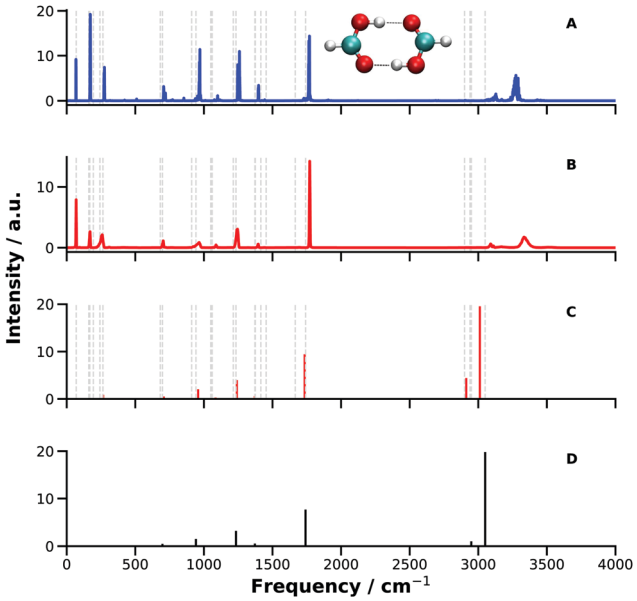

Fig. 4 Infrared spectrum of FAD obtained from the PES_{MP2} (panel A) and from the PES_{TL} (panel B) using finite-*T* simulations (A and B) and the VPT2 approach (C). The results are complemented with experimental frequencies[33,36] and intensities for 7 fundamentals[104] (D). Six intensities of ref. 104 were estimated based on experimental data from ref. 105 and extended with one intensity from ref. 106. Experimentally, the intensity of the OH stretch is distributed over a much wider frequency range.[30] The gray dashed lines indicate the positions of the observed fundamental frequencies. The finite-*T* spectra (IR) are calculated from the dipole–dipole auto-correlation function of 1000 MDs each run for 200 ps with the PES_{MP2} and PES_{TL} at 300 K.

Alternatively, reduced-dimensionality (RD) approaches such as RD-VPT2 exist.[99]

3.4 Finite-*T* infrared spectra

Formic acid monomer. The IR spectra for FAM obtained from MD simulations on PES_{MP2} and PES_{TL} are shown in Fig. 3 together with the experimental frequencies.[29,39] The low frequency modes faithfully describe those measured experimentally. On the other hand, the computed high frequency X–H modes are consistently shifted to the blue by 150 to 200 cm^{-1} relative to experiment. It is known that specifically for high-frequency modes the anharmonic regions of the PES are not sufficiently sampled in finite-*T* MD simulations.[43,44,100] This usually leads to overestimation of computed frequencies when compared with experiments as is also found here. The OH stretch frequency for FAM using PES_{MP2} and PES_{TL} is centered around the same frequency of 3750 cm^{-1} which compares with an experimental value of 3571 cm^{-1}.[29] Counter to the expectation that on a higher-level PES agreement between computation and experiment improves, PES_{MP2} and PES_{TL} find the OH stretch mode at essentially the same frequency. In this particular case this is not surprising as the harmonic *ab initio* OH stretch frequencies of FAM at the MP2 and CCSD(T) levels of theory are already within 1 cm^{-1}, see Table S4 (ESI†). Hence, the inferior performance of MD simulations for the high-frequency XH stretch modes is not primarily related to the quality of the PES but rather due to shortcomings of finite-temperature MD simulations to realistically sample the anharmonicity of the PES.

Formic acid dimer. The averaged IR spectrum from 1000 independent trajectories, each 200 ps in length, using PES_{MP2} and PES_{TL} for FAD is shown in Fig. 4. For the modes below 2000 cm^{-1} the position and the relative intensities from the computations compare favourably with experiments.[33,36] Even finer details, such as the low intensities of the peaks at 942 and 1233.9 cm^{-1} are surprisingly well captured by simulations with the two PESs. It is also of interest to note that for some modes the computed harmonic, anharmonic and experimentally observed frequencies agree rather well. For example, for the lowest frequency mode of FAD $\omega(PES_{TL})$ = 69.5, $\nu(MD(PES_{TL}))$ = 68.7, and $\nu(Exp)$ = 69.2 cm^{-1}.[30] Larger differences between the predicted frequencies and experiment are, however, again found in the high frequency range. Based on the normal modes, an OH stretch frequency of 3273 and of 3338 cm^{-1} is found in the IR of the FAD on PES_{MP2} and PES_{TL}, respectively. The agreement between experiment and simulations is similar to that found from 12 ps simulations on the PIP-based PES although there the 1741 cm^{-1} band appears to be shifted somewhat to the blue.[44]

The experimental Fourier Transform transmittance spectrum of FAD recorded in a jet reported[30] a broad band with superimposed sharp features extending from below 2600 cm^{-1} up to at least 3300 cm^{-1}. The sharp features arise mostly from combination bands and make it difficult to assign one specific absorption feature to the OH stretch vibration. However, it is reasonable to assume that it is located to the blue side of the CH-stretch band rather than to the red side of it. Interestingly, the width of the jet-cooled spectrum is comparable to that recorded at room temperature. Hence, cooling only leads to sharpening of certain features but not to a simpler spectrum. This is consistent with other studies on formic and acetic acid.[31,101] A potential assignment of the OH stretch vibration in FAD was made[30] to a signature at 3084 cm^{-1} by comparing with earlier calculations (SCF with double zeta basis set).[102] Similarly, earlier Raman spectra of $(DCOOH)_2$ reported a broad absorption around and above 3000 cm^{-1} and assigned features between 2565 cm^{-1} and 3427 cm^{-1} to the dimer OH stretching band.[103] Finally, a broad absorption was also found from lower resolution, room temperature IR spectroscopy[34] for which spectral subtraction techniques were used to obtain the IR spectrum of FAD. The transition assigned to the OH-stretch was the region between 2600 and 3400 cm^{-1} with a maximum at ~3100 cm^{-1}.[34] Hence, assignment of the OH-stretch frequency is not straightforward. Here, a position of 3050 ± 100 cm^{-1} was used to compare with. However, it needs to be stressed that considerable uncertainty about both, the position and the width of this band exist.

The failure of finite-*T* MD simulations to even qualitatively capture the spectroscopy of high-frequency modes is primarily related to the fact that at $T \sim 300$ K, at which most MD studies are carried out, the anharmonicities of X–H vibrations are not sampled adequately. Because constraining the correct amount of ZPE in the modes of polyatomic molecules is as of now an unsolved problem,[43] an alternative that has been considered is

 This journal is © the Owner Societies 2022

Open Access Article. Published on 26 October 2021. Downloaded on 2/16/2026 3:25:57 PM. This article is licensed under a Creative Commons Attribution-NonCommercial 3.0 Unported Licence.

Table 2 VPT2 anharmonic frequencies (in cm^{-1}) for FAM and FAD calculated using PhysNet trained on MP2 data (PES_{MP2}) and transfer learned to CCSD(T) (PES_{TL}) quality. They are compared to their reference *ab initio* values (MP2) and to experiment ([a]ref. 50 and references therein; [b]ref. 30; [c]ref. 32; [d]ref. 33; [e]ref. 93; [f]ref. 94; [g]ref. 51; [h]ref. 95; [i]ref. 59; [j]ref. 61; [k]ref. 96; [l]ref. 28). The MAEs of PES_{MP2} and PES_{TL} are given with respect to the *ab initio* MP2 and experimental values, respectively. Mode 14 of FAD is involved in a strong resonance triad from which a frequency of 1233.9 cm^{-1} is assigned to the fundamental. Note that the symmetry of the VPT2 frequencies marked with a * does not correspond to the assignments of the experimental frequencies (see, *e.g.* ref. 30 or ref. 97). The MAEs of the FAD frequencies of PES_{MP2} and MP2 with respect to experiment are 22.0 and 18.6 cm^{-1}, respectively. The MAEs of the PES_{TL} frequencies below 2000 cm^{-1} are 6.7 and 17.1 cm^{-1} for FAM and FAD, respectively

	FAM				FAD			
	PES_{MP2}	MP2	PES_{TL}	Exp[a]	PES_{MP2}	MP2	PES_{TL}	Exp
1	619.9	619.5	621.6	626.17	78.0	70.2	91.6	69.2[b]
2	643.0	641.8	632.2	640.73	178.5	160.4	164.4	161.0[c]
3	1036.7	1036.4	1029.1	1033.47	185.0	171.0	200.9	168.5[b]
4	1097.2	1098.2	1098.6	1104.85	206.2	197.3	229.4	194.0[c]
5	1222.2	1220.6	1296.0	1306.2	255.8	246.0	265.8	242.0[c]
6	1380.7	1381.0	1374.9	1379.05	281.1	271.9	327.6	264.0[d]
7	1761.3	1760.5	1768.2	1776.83	686.4	678.5	679.6	682.0[c]
8	2975.4	2967.8	2935.3	2942.06	713.4	707.6	707.4	698.0[b]
9	3549.8	3554.9	3548.3	3570.5	945.2	936.0	925.6	911.0[e]
10					971.6	966.1	958.1	942[f]
11					1065.2*	1062.6	1075.4	1050[g]
12					1083.9*	1076.6	1084.6	1060[h]
13					1237.1	1233.0	1238.2	1214[h]
14					1238.4	1240.6	1240.1	1233.9[i]
15					1370.4	1369.2	1371.2	1371.78[i]
16					1376.7	1373.2	1374.4	1375[h]
17					1403.0*	1407.6	1406.6	1415[g]
18					1426.7*	1430.7	1435.0	1454[b]
19					1662.6	1659.1	1661.6	1666[k]
20					1732.9	1732.9	1734.5	1741[k]
21					2763.0*	2763.5	2875.0	2900[d]
22					2945.4*	2961.7	2912.3	2939.7[l]
23					2961.8	2962.9	2920.1	2949[h]
24					2968.5	2963.4	3011.2	3050[b]
MAE	**2.0**		**8.4**		**6.4**		**19.3**	

to run MD simulations at higher temperature.[43,100] Here, simulations with increasing amount of energy in the OH stretch of FAM and FAD have been carried out using PES_{TL}. The *NVE* simulations are run with excess energies of 0.1, 0.3, 0.6, and 0.9 eV for FAM and of 0.1 and 0.3 eV for FAD in each of the OH stretch modes. For comparison, the (harmonic) ZPE of FAM in this mode is 1647 cm^{-1} (equivalent to 0.2 eV). This energy is initially placed into the OH stretch(es) as kinetic energy. The *E*-dependent IR spectra (Fig. 5) correspond to an ensemble of 45 trajectories run for 200 ps each. For FAM it was found that with increasing energy content in the OH stretch the associated band shifts progressively towards the red as expected. With an excess of 0.5 eV the computed OH stretch aligns with that reported from experiment.

Even though the energy redistribution to the lower frequency modes does occur on the time scale of the simulations the spectroscopic features below 2000 cm^{-1} do not respond strongly to the increased temperature. To assess the redistribution of vibrational energy a supplemental trajectory is run for FAM with an excess of 0.5 eV in the OH stretch mode. The energy remains in this mode for at least 150 ps after which it slowly redistributes into other degrees of freedom, see Fig. S1 (ESI†).

For FAD running the simulations at higher temperature apparently does not solve the problem of overestimating the location of the XH bands. As one additional complication, the binding energy, *i.e.* $E_{FAD} - 2E_{FAM}$, of the dimer is only −16.79 kcal mol^{-1} (−0.73 eV). Hence, excitation of the two OH stretch vibrations with more than ∼8.5 kcal mol^{-1} (∼0.35 eV) leads to dissociation of the dimer and the spectroscopy of the H-bonded OH···O motifs can not be probed. For the simulations with 0.1 eV of excess the OH···O hydrogen bond (distance between O_{10} and H_5 or O_2 and H_6, see Fig. 1) extends up to 2.3 Å compared with an equilibrium separation of 1.68 Å. With an excess of 0.3 eV the two OH···O ''bonds'' elongate up to 3.3 Å. This indicates considerable destabilization of the dimer due to partial breaking of the hydrogen bonds and the two FAMs in the dimer start to behave more like monomers without fully dissociating FAD. Loosening the OH···O contact affects, however, the vibrational frequency of the OH stretch. Visual inspection also shows that an out of plane bending motion of the two monomers is excited due to vibrational energy redistribution which further weakens the OH···O hydrogen bond. For the simulations of FAD with 0.3 eV excess the OH stretch shifts to the blue by ∼70 cm^{-1} whereas the CH stretch shifts to the red as expected for simulations at higher temperature.

3.5 Diffusion Monte Carlo and binding energy D_0

The ML PESs can also be used to determine the dissociation energy D_0 of FAD from computations. For this, a high-quality estimate for the total ZPE for FAM and FAD is required which can be obtained from DMC simulations. The average ZPE from

Open Access Article. Published on 26 October 2021. Downloaded on 2/16/2026 3:25:57 PM.
This article is licensed under a Creative Commons Attribution-NonCommercial 3.0 Unported Licence.

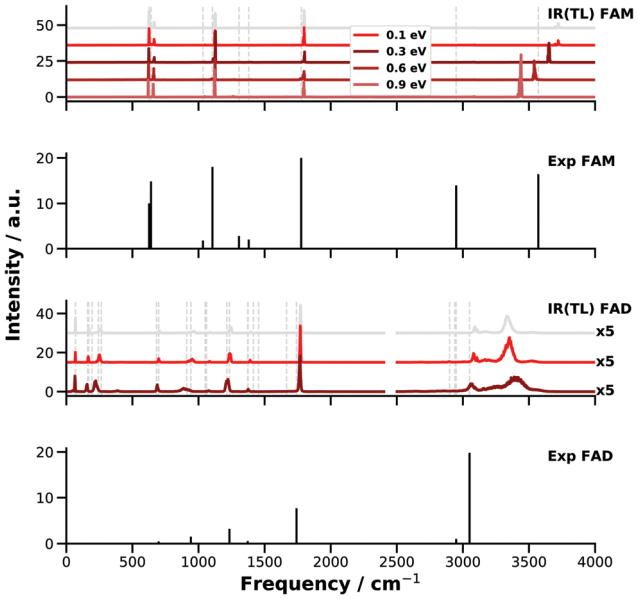

Fig. 5 IR spectra from E-dependent MD simulations for FAM and FAD with PES_{TL}. For comparison, for FAM the harmonic ZPE of the OH stretch is 0.23 eV and the total ZPEs are ~0.9 and 1.9 eV. The grey vertical lines mark the peak positions of the experiments[29,39] and the grey spectra are calculated from room temperature simulations on PES_{TL} (see Fig. 3 and 4). For FAM a clear energy dependence is seen: the OH peak ~3725 cm^{-1} with an energy of 0.1 eV shifts to the red and reaches ~3435 cm^{-1} with an energy of 0.9 eV. This energy dependence was not achieved for FAD, for which the OH stretch peak was mainly broadened and blue shifted for 0.3 eV. In contrast, the C–H peak is red shifted as expected. For FAD, the IR signals above 2500 cm^{-1} are scaled by a factor of 5 for better visibility.

10 independent DMC simulations for FAM using the PES_{TL} is 20.932 ± 0.033 kcal mol^{-1} (7321.1 ± 11.5 cm^{-1}). Similarly for FAD a ZPE of 43.741 ± 0.013 kcal mol^{-1} (15298.9 ± 4.5 cm^{-1}) was found. The average DMC energies and standard deviations are determined from block averaging.[107] These ZPEs (accounting for anharmonicity) compare also favourably with 20.900 and 43.885 kcal mol^{-1}, respectively, for the monomer and the dimer from the VPT2 calculations using the same PES (PES_{TL}). Similarly, the result for FAD also agrees well with a recent study using a PES based on permutationally invariant polynomials at the CCSD(T)-F12a/haTZ level of theory and DMC calculations which reported a ZPE of 15 337 ± 7 cm^{-1} (43.850 ± 0.020 kcal mol^{-1}).[40]

Based on these ZPEs the FAD dissociation energy $D_0 = D_e^C - 2ZPE_{FAM} + ZPE_{FAD}$ can be determined. Here, D_e^C is the corrected (see below) binding energy (“from the bottom of the potential”) and ZPE_{FAM} and ZPE_{FAD} are the ZPEs of FAM and FAD, respectively. The dissociation energy D_e needs to be corrected (a) to account for basis set superposition error (BSSE) and (b) to include effects due to finite-size basis set effects by extrapolation to the complete basis set (CBS) limit. These corrections were determined in previous work[38] and will be used here. This is possible because D_e = −16.79 kcal mol^{-1} from the present work for dissociation of FAD into two FAMs each at their respective equilibrium structure, is identical to the value reported from the earlier CCSD(T)/aug-cc-pVTZ calculations.[38] Including corrections for BSSE at the CBS limit yields D_e^C = −16.11 kcal mol^{-1}.[38] Together with the ZPEs of FAM and FAD determined above this yields a best estimate of D_0 = −14.23 ± 0.08 kcal mol^{-1} where the error is that of the ZPEs from the DMC calculations. This value is consistent, within error bars, with the experimentally reported value of −14.22 ± 0.12 kcal mol^{-1} [33] and compares with D_0 = −14.3 ± 0.1 kcal mol^{-1} from computations with ZPEs obtained from a hybrid VPT2 approach (harmonic frequencies from CCSD(T)/AVQZ and correcting for anharmonic effects using MP2/AVDZ).[38]

4 Discussion and conclusion

In this work the harmonic and anharmonic vibrational spectra for FAM and FAD in the gas phase have been determined based on correctly dissociating machine-learned PESs at the MP2 level of theory and transfer-learned to the CCSD(T) level of theory with the aug-cc-pVTZ basis set. Harmonic frequencies on PES_{MP2} and PES_{TL} from diagonalizing the Hessian are in good agreement with those determined from conventional *ab initio* calculations. Accounting for anharmonicity in the vibrations through VPT2 calculations yields spectra in good agreement with those observed experimentally. The finite-temperature MD simulations find good agreement with experimental spectra for all modes below 2000 cm^{-1} but disagree by several 100 cm^{-1} for the high-frequency XH stretch vibrations. This confirms earlier findings and is related to the fact that MD simulations at 300 K do not sample the mechanical anharmonicity of XH stretch or any other strongly anharmonic modes sufficiently to give reliable frequencies from such an approach. Contrary to that, a 24-mode VSCF/VCI calculation on a PES calculated at the CCSD(T)-F12a/haTZ level of theory and fit to permutationally invariant polynomials[40] correctly describes the spectroscopy and increased width of the OH-stretch band.[43]

The present work also allows to make contact with a recent assessment[35] of various sources of errors in the spectroscopy and thermodynamics of FAD which reported that “More often than not, the overestimation of harmonic downshifts in DFT is qualitatively compensated by the inability of classical dynamics to sample the anharmonic region probed by the quantum nature of the hydrogen atom. This frequently provides right answers for the wrong reasons whenever high-frequency XH stretching spectra are simulated, because in this case, temperatures of several 1000 K would be needed to sample the relevant fundamental vibrational displacements.” While some of these statements are supported by the present results, others require amendments.

In agreement with this assessment the present work finds that energies up to 0.5 eV (~5800 K) are required for the OH stretch vibration in FAM to agree with experiment. This is consistent with the temperature $T = \frac{hc\omega_e}{k}$ required to reproduce the stretching fundamental of a simple Morse oscillator with harmonic wavenumber ω_e.[108] On the other hand, the CCSD(T)-level quality of PES_{TL} allows to probe whether or not accidental agreement with experiment is found for the

 This journal is © the Owner Societies 2022

Open Access Article. Published on 26 October 2021. Downloaded on 2/16/2026 3:25:57 PM.
This article is licensed under a Creative Commons Attribution-NonCommercial 3.0 Unported Licence.

Table 3 OH stretch frequencies of FAM and FAD obtained from *ab initio* harmonic frequency calculations (ω(MP2) and ω(CCSD(T))), from MD simulations at 300 K on PES_{MP2} (ν(MP2)) and PES_{TL} (ν(TL)), and from VPT2 calculations using PES_{TL}, compared with experiment ([a]ref. 50; [b]ref. 30). CCSD(T) frequencies for the dimer are from ref. 38 and 36 and were calculated using the AVTZ and AVQZ basis sets, respectively. The position of the H-transfer band (3050 ± 100[b]) is an estimate based on ref. 30, see also discussion in the text

[cm^{-1}]	ω(MP2)	ω(CCSD(T))	ν(MP2)	ν(TL)	VPT2(TL)	Exp.
OH (FAM)	3741	3742	3750	3750	3548	3571[a]
OH (FAD)	3230	3309[36]/3306[38]	3273	3338	3011	3050 ± 100[b]
Δ	−511	−433	−477	−412	−537	-521 ± 100

complexation induced red shifts $\Delta\omega$ and $\Delta\nu$. For the harmonic frequencies, the red shifts are $\Delta\omega = -511$ cm^{-1} and $\Delta\omega = -433$ cm^{-1} from normal mode calculations at the MP2 and CCSD(T) levels of theory, compared with −518 and −449 cm^{-1} from normal modes on the respective NN-learned PES_{MP2} and PES_{TL}, see Tables S4 and S5 (ESI†). MD simulations with PES_{MP2} at 300 K find $\Delta\nu = -477$ cm^{-1} compared with -521 ± 100 cm^{-1} estimated from experiments,[30] see Table 3. With PES_{TL} the red shift is $\Delta\nu = -412$ cm^{-1} and the VPT2 calculations yield a shift of −537 cm^{-1}. It should be noted that VPT2 calculations are known to have limitations for proton bound dimers.[98] This is also consistent with the present finding that the ZPEs of FAD from DMC simulations and VPT2 calculations using PES_{TL} differ by 0.14 kcal mol^{-1} (50 cm^{-1}) whereas that for FAM is virtually identical.

The shifts from finite-T MD simulations still suffer from the limitation that the anharmonicity of the OH stretch is not sufficiently sampled, irrespective of the level of theory at which the PES was determined. However, it is likely that the magnitude and the direction of the error in the anharmonic OH stretch frequencies differ for FAM compared with FAD. This can be seen most clearly in Fig. 5 where the OH stretch in FAM/FAD shifts to the red/blue with increasing internal energy, respectively. The complexation induced red shift from simulations on PES_{MP2} is within 44 cm^{-1} of the experimentally observed value whereas that on (higher-level) PES_{TL} is lower by 109 cm^{-1}. Given the close agreement for the anharmonic OH-stretch for FAM from simulations on the two PESs it is expected that PES_{TL} for FAD is of similar quality as for FAM and only minor improvement is expected by adding additional reference points in the transfer learning. This is supported by the finding that for the OH stretch $\Delta\omega$ from MP2 calculations differs from that on PES_{MP2} by 7 cm^{-1} whereas for CCSD(T) and PES_{TL} the difference is 16 cm^{-1}. Likewise, using a larger basis set, such as aug-cc-pVQZ, is unlikely to change ω and ν of the OH stretch appreciably because the harmonic frequencies from CCSD(T)/aug-cc-pVTZ and CCSD(T)/aug-cc-pVQZ differ only by 3 cm^{-1}, see Table 3. Thus, the apparent "agreement" between experiment and spectra computed from the present MD simulations on PES_{MP2} is due to differential undersampling the anharmonicity of the OH coordinate at 300 K for FAM and FAD and also due to the uncertainty in assigning the OH-stretch in FAD more definitively.

This changes as soon as DPT occurs, because then the full anharmonicity of the energy function along the XH coordinate must be sampled. From simulations with multiple forward and backward crossings in the MD simulations it is expected that the anharmonicity is comprehensively sampled which should provide more realistic IR spectra. Previous work on FAD accomplished this by using the Molecular Mechanics with Proton Transfer (MMPT)[109] PES for which trajectories 250 ns in length were carried out which sampled 25 DPT events.[34] Such long simulation times become accessible because these energy functions can be evaluated at the speed of a conventional empirical force field. Furthermore, the MMPT function used did not allow FAD to dissociate into two monomers.

In summary, the present work uses machine-learned, full dimensional and reactive PESs at the MP2 and CCSD(T) levels of theory for FAM and FAD to characterize their vibrational dynamics. It is established that for framework vibrational modes (below 2000 cm^{-1}) computed frequencies from VPT2 and finite-T MD simulations agree well with experiments. However, for the high-frequency XH stretch modes – in particular the OH modes – MD simulations do not sufficiently sample the anharmonicities which leads to a considerable overestimation of the experimentally observed frequencies. Hence, it is primarily the use of MD simulations that is the source of errors for the disagreement between experiments and simulations. The estimated experimentally observed red shift of -521 ± 100 cm^{-1} for the OH stretch peak[30] compares with −477 cm^{-1} from finite-T simulations on PES_{MP2} and −412 cm^{-1} when using PES_{TL} in the simulations. The red shift from the VPT2 calculations is −537 cm^{-1}. However, there is considerable uncertainty on the position and width of the OH-stretch fundamental which makes it less suited for direct comparison with computations.

For FAM, running simulations at elevated temperatures does not affect the framework modes but shifts the OH stretch modes towards the frequencies observed in experiments. On the other hand, for FAD destabilization of the dimer prevents using such an approach. Hence, computing accurate complexation-induced spectral shifts remain a challenge even on high-level PESs due to shortcomings in the dynamics simulations underlying the spectroscopy. This is also not expected to change if approximate quantum methods such as quasiclassical MD (QCMD) or ring-polymer MD (RPMD) simulations are used, as was shown explicitly.[44,100] The computed dissociation energy of $D_0 = -14.23 \pm 0.08$ kcal mol^{-1} from a combination of electronic structure calculations and DMC simulations on the CCSD(T)-quality PES_{TL} is in favourable agreement with the value of -14.22 ± 0.1 kcal mol^{-1} from experiments.

Full-dimensional PESs for medium-sized molecules as the one used here provide an ideal starting point for the accurate exploration of molecular motions. Notable efforts in this direction include a PIP-based PES for 15-atom tropolone[110] or reproducing kernel Hilbert space (RKHS)-based representations for molecular systems up to 10 atoms.[111] For the motion of H_2 in hydrates, which is inherently a high-dimensional

Open Access Article. Published on 26 October 2021. Downloaded on 2/16/2026 3:25:57 PM.
This article is licensed under a Creative Commons Attribution-NonCommercial 3.0 Unported Licence.

problem, an NN-based energy function has been successfully developed to follow quantum diffusion.[112] Similarly, NN-based energy functions have been used for accurate spectroscopic studies of van der Waals complexes such as HCl–H_2O and its isotopologues.[113] Finally, NN-based energy functions have also been used for bond-forming/bond-breaking processes.[67,114] These developments together with suitable embedding in surrounding environments provide considerable scope to more quantitatively characterize challenging problems in physical chemistry at molecular-level detail.

Data availability statement

The MP2 and CCSD(T) datasets are available on Zenodo (https://doi.org/10.5281/zenodo.5583206) and the PhysNet codes can be downloaded from github (https://github.com/MMunibas/PhysNet).

Conflicts of interest

There are no conflicts of interest to declare.

Acknowledgements

We thank Prof. J. M. Bowman and Dr C. Qu for fruitful exchange on the implementation of DMC and Prof. M. Suhm and Dr A. Nejad for valuable correspondence. This work was supported by the Swiss National Science Foundation through grants 200021-117810, 200020-188724 and the NCCR MUST, and the University of Basel.

References

1 T. R. Rizzo, J. A. Stearns and O. V. Boyarkin, Spectroscopic studies of cold, gas-phase biomolecular ions, *Int. Rev. Phys. Chem.*, 2009, **28**, 481–515.
2 K. El Hage, S. Brickel, S. Hermelin, G. Gaulier, C. Schmidt, L. Bonacina, S. C. Van Keulen, S. Bhattacharyya, M. Chergui and P. Hamm, *et al.*, Implications of short time scale dynamics on long time processes, *Struct. Dyn.*, 2017, **4**, 061507.
3 C. R. Baiz, B. Błasiak, J. Bredenbeck, M. Cho, J.-H. Choi, S. A. Corcelli, A. G. Dijkstra, C.-J. Feng, S. Garrett-Roe and N.-H. Ge, *et al.*, Vibrational spectroscopic map, vibrational spectroscopy, and intermolecular interaction, *Chem. Rev.*, 2020, **120**, 7152–7218.
4 Z. Getahun, C. Huang, T. Wang, B. De Leon, W. DeGrado and F. Gai, Using nitrile-derivatized amino acids as infrared probes of local environment, *J. Am. Chem. Soc.*, 2003, **125**, 405–411.
5 S. M. Salehi, D. Koner and M. Meuwly, Dynamics and infrared spectroscopy of monomeric and dimeric wild type and mutant insulin, *J. Phys. Chem. B*, 2020, **124**, 11882–11894.
6 J. M. Schmidt-Engler, L. Blankenburg, B. Blasiak, L. J. G. W. van Wilderen, M. Cho and J. Bredenbeck, Vibrational lifetime of the SCN protein label in H2O and D_2O reports site-specific solvation and structure changes during PYP's photocycle, *Anal. Chem.*, 2020, **92**, 1024–1032.
7 S. M. Salehi and M. Meuwly, Site-selective dynamics of azidolysozyme, *J. Chem. Phys.*, 2021, **154**, 165101.
8 H. T. Turan and M. Meuwly, Spectroscopy, dynamics, and hydration of S-nitrosylated myoglobin, *J. Phys. Chem. B*, 2021, **125**, 4262–4273.
9 R. Bloem, K. Koziol, S. A. Waldauer, B. Buchli, R. Walser, B. Samatanga, I. Jelesarov and P. Hamm, Ligand Binding Studied by 2D IR Spectroscopy Using the Azidohomoalanine Label, *J. Phys. Chem. B*, 2012, **116**, 13705–13712.
10 P. Mondal and M. Meuwly, Vibrational Stark spectroscopy for assessing ligand-binding strengths in a protein, *Phys. Chem. Chem. Phys.*, 2017, **19**, 16131–16143.
11 D. Koner, R. J. Bemish and M. Meuwly, Dynamics on multiple potential energy surfaces: quantitative studies of elementary processes relevant to hypersonics, *J. Phys. Chem. A*, 2020, **124**, 6255–6269.
12 M. Meuwly, Machine learning for chemical reactions, *Chem. Rev.*, 2021, **121**, 10218–10239.
13 O. T. Unke, S. Chmiela, H. E. Sauceda, M. Gastegger, I. Poltavsky, K. T. Schütt, A. Tkatchenko and K.-R. Müller, Machine learning force fields, *Chem. Rev.*, 2021, **121**(16), 10142–10186.
14 C. Qu, P. L. Houston, R. Conte, A. Nandi and J. M. Bowman, Breaking the coupled cluster barrier for machine-learned potentials of large molecules: The case of 15-atom acetylacetone, *J. Phys. Chem. Lett.*, 2021, **12**, 4902–4909.
15 R. A. Friesner, *Ab initio* quantum chemistry: Methodology and applications, *Proc. Natl. Acad. Sci. U. S. A.*, 2005, **102**, 6648–6653.
16 S. J. Pan and Q. Yang, A survey on transfer learning, *IEEE Trans. Knowledge Data Eng.*, 2009, **22**, 1345–1359.
17 M. E. Taylor and P. Stone, Transfer learning for reinforcement learning domains: A survey, *J. Mach. Learn. Res.*, 2009, **10**, 1633–1685.
18 J. S. Smith, B. T. Nebgen, R. Zubatyuk, N. Lubbers, C. Devereux, K. Barros, S. Tretiak, O. Isayev and A. E. Roitberg, Approaching coupled cluster accuracy with a general-purpose neural network potential through transfer learning, *Nat. Commun.*, 2019, **10**, 1–8.
19 R. Ramakrishnan, P. Dral, M. Rupp and O. A. von Lilienfeld, Big data meets quantum chemistry approximations: The Δ-machine learning approach, *J. Chem. Theory Comput.*, 2015, **11**, 2087–2096.
20 S. Käser, O. T. Unke and M. Meuwly, Reactive dynamics and spectroscopy of hydrogen transfer from neural network-based reactive potential energy surfaces, *New J. Phys.*, 2020, **22**, 055002.
21 S. Käser, D. Koner, A. S. Christensen, O. A. von Lilienfeld and M. Meuwly, Machine learning models of vibrating H_2CO: Comparing reproducing kernels, FCHL, and PhysNet, *J. Phys. Chem. A*, 2020, **124**, 8853–8865.
22 A. Nandi, C. Qu, P. L. Houston, R. Conte and J. M. Bowman, Δ-machine learning for potential energy

Open Access Article. Published on 26 October 2021. Downloaded on 2/16/2026 3:25:57 PM. This article is licensed under a Creative Commons Attribution-NonCommercial 3.0 Unported Licence.

surfaces: A PIP approach to bring a DFT-based PES to CCSD(T) level of theory, *J. Chem. Phys.*, 2021, **154**, 051102.
23 S. Käser, E. D. Boittier, M. Upadhyay and M. Meuwly, Transfer learning to CCSD(T): Accurate anharmonic frequencies from machine learning models, *J. Chem. Theory Comput.*, 2021, **17**, 3687–3699.
24 P. Khare, N. Kumar, K. Kumari and S. Srivastava, Atmospheric formic and acetic acids: An overview, *Rev. Geophys.*, 1999, **37**, 227–248.
25 R. van Putten, T. Wissink, T. Swinkels and E. A. Pidko, Fuelling the hydrogen economy: Scale-up of an integrated formic acid-to-power system, *Int. J. Hydrogen Energy*, 2019, **44**, 28533–28541.
26 Q. Wang, J. Warnan, S. Rodrguez-Jiménez, J. J. Leung, S. Kalathil, V. Andrei, K. Domen and E. Reisner, Molecularly engineered photocatalyst sheet for scalable solar formate production from carbon dioxide and water, *Nat. Energy*, 2020, **5**, 703–710.
27 C. Xia, P. Zhu, Q. Jiang, Y. Pan, W. Liang, E. Stavitski, H. N. Alshareef and H. Wang, Continuous production of pure liquid fuel solutions via electrocatalytic CO_2 reduction using solid-electrolyte devices, *Nat. Energy*, 2019, **4**, 776–785.
28 F. Ito and T. Nakanaga, A jet-cooled infrared spectrum of the formic acid dimer by cavity ring-down spectroscopy, *Chem. Phys. Lett.*, 2000, **318**, 571–577.
29 M. Freytes, D. Hurtmans, S. Kassi, J. Liévin, J. Vander Auwera, A. Campargue and M. Herman, Overtone spectroscopy of formic acid, *Chem. Phys.*, 2002, **283**, 47–61.
30 R. Georges, M. Freytes, D. Hurtmans, I. Kleiner, J. Vander Auwera and M. Herman, Jet-cooled and room temperature FTIR spectra of the dimer of formic acid in the gas phase, *Chem. Phys.*, 2004, **305**, 187–196.
31 P. Zielke and M. Suhm, Raman jet spectroscopy of formic acid dimers: low frequency vibrational dynamics and beyond, *Phys. Chem. Chem. Phys.*, 2007, **9**, 4528–4534.
32 Z. Xue and M. Suhm, Probing the stiffness of the simplest double hydrogen bond: The symmetric hydrogen bond modes of jet-cooled formic acid dimer, *J. Chem. Phys.*, 2009, **131**, 054301.
33 F. Kollipost, R. W. Larsen, A. V. Domanskaya, M. Nörenberg and M. A. Suhm, Communication: The highest frequency hydrogen bond vibration and an experimental value for the dissociation energy of formic acid dimer, *J. Chem. Phys.*, 2012, **136**, 151101.
34 K. Mackeprang, Z.-H. Xu, Z. Maroun, M. Meuwly and H. G. Kjaergaard, Spectroscopy and dynamics of double proton transfer in formic acid dimer, *Phys. Chem. Chem. Phys.*, 2016, **18**, 24654–24662.
35 A. Nejad and M. A. Suhm, Concerted pair motion due to double hydrogen bonding: The formic acid dimer case, *J. Ind. Inst. Sci.*, 2020, **100**, 5–19.
36 R. Kalescky, E. Kraka and D. Cremer, Local vibrational modes of the formic acid dimer-the strength of the double hydrogen bond, *Mol. Phys.*, 2013, **111**, 1497–1510.
37 S. D. Ivanov, I. M. Grant and D. Marx, Quantum free energy landscapes from ab initio path integral metadynamics: Double proton transfer in the formic acid dimer is concerted but not correlated, *J. Chem. Phys.*, 2015, **143**, 124304.
38 E. Miliordos and S. S. Xantheas, On the validity of the basis set superposition error and complete basis set limit extrapolations for the binding energy of the formic acid dimer, *J. Chem. Phys.*, 2015, **142**, 094311.
39 D. P. Tew and W. Mizukami, *Ab initio* vibrational spectroscopy of *cis*-and *trans*-formic acid from a global potential energy surface, *J. Phys. Chem. A*, 2016, **120**, 9815–9828.
40 C. Qu and J. M. Bowman, An *ab initio* potential energy surface for the formic acid dimer: Zero-point energy, selected anharmonic fundamental energies, and ground-state tunneling splitting calculated in relaxed 1–4-mode subspaces, *Phys. Chem. Chem. Phys.*, 2016, **18**, 24835–24840.
41 J. O. Richardson, Full-and reduced-dimensionality instanton calculations of the tunnelling splitting in the formic acid dimer, *Phys. Chem. Chem. Phys.*, 2017, **19**, 966–970.
42 C. Qu and J. M. Bowman, High-dimensional fitting of sparse datasets of CCSD(T) electronic energies and MP2 dipole moments, illustrated for the formic acid dimer and its complex IR spectrum, *J. Chem. Phys.*, 2018, **148**, 241713.
43 C. Qu and J. M. Bowman, Quantum and classical IR spectra of $(HCOOH)_2$, $(DCOOH)_2$ and $(DCOOD)_2$ using ab initio potential energy and dipole moment surfaces, *Faraday Discuss.*, 2018, **212**, 33–49.
44 C. Qu and J. M. Bowman, IR spectra of $(HCOOH)_2$ and $(DCOOH)_2$: Experiment, VSCF/VCI, and ab initio molecular dynamics calculations using full-dimensional potential and dipole moment surfaces, *J. Phys. Chem. Lett.*, 2018, **9**, 2604–2610.
45 F. Richter and P. Carbonnière, Vibrational treatment of the formic acid double minimum case in valence coordinates, *J. Chem. Phys.*, 2018, **148**, 064303.
46 W. Reutemann and H. Kieczka, *Ullmann's Encyclopedia of Industrial Chemistry*, American Cancer Society, 2011.
47 R. M. Balabin, Polar (acyclic) isomer of formic acid dimer: Gas-phase Raman spectroscopy study and thermodynamic parameters, *J. Phys. Chem. A*, 2009, **113**, 4910–4918.
48 R. C. Millikan and K. S. Pitzer, Infrared spectra and vibrational assignment of monomeric formic acid, *J. Chem. Phys.*, 1957, **27**, 1305–1308.
49 G. Luiz, A. Scalabrin and D. Pereira, Gas phase infrared Fourier transform spectra of $H^{12}COOH$ and $H^{13}COOH$, *Infrared Phys. Technol.*, 1997, **38**, 45–49.
50 A. Nejad, M. A. Suhm and K. A. Meyer, Increasing the weights in the molecular work-out of cis- and trans-formic acid: Extension of the vibrational database via deuteration, *Phys. Chem. Chem. Phys.*, 2020, **22**, 25492–25501.
51 R. C. Millikan and K. S. Pitzer, The infrared spectra of dimeric and crystalline formic acid, *J. Am. Chem. Soc.*, 1958, **80**, 3515–3521.
52 F. Ito and T. Nakanaga, Jet-cooled infrared spectra of the formic acid dimer by cavity ring-down spectroscopy: observation of the O-H stretching region, *Chem. Phys.*, 2002, **277**, 163–169.
53 K. A. Meyer, J. A. Davies and A. M. Ellis, Shifting formic acid dimers into perspective: vibrational scrutiny in

Open Access Article. Published on 26 October 2021. Downloaded on 2/16/2026 3:25:57 PM.
This article is licensed under a Creative Commons Attribution-NonCommercial 3.0 Unported Licence.

helium nanodroplets, *Phys. Chem. Chem. Phys.*, 2020, **22**, 9637–9646.
54 A. Aerts, P. Carbonnière, F. Richter and A. Brown, Vibrational states of deuterated trans- and cis-formic acid: DCOOH, HCOOD, and DCOOD, *J. Chem. Phys.*, 2020, **152**, 024305.
55 A. Nejad and E. L. Sibert III, The Raman jet spectrum of trans-formic acid and its deuterated isotopologs: Combining theory and experiment to extend the vibrational database, *J. Chem. Phys.*, 2021, **154**, 064301.
56 Y. Kim, Direct dynamics calculation for the double proton transfer in formic acid dimer, *J. Am. Chem. Soc.*, 1996, **118**, 1522–1528.
57 S. Miura, M. E. Tuckerman and M. L. Klein, An ab initio path integral molecular dynamics study of double proton transfer in the formic acid dimer, *J. Chem. Phys.*, 1998, **109**, 5290–5299.
58 M. Ortlieb and M. Havenith, Proton transfer in $(HCOOH)_2$: An IR high-resolution spectroscopic study of the antisymmetric C-O stretch, *J. Phys. Chem. A*, 2007, **111**, 7355–7363.
59 K. G. Goroya, Y. Zhu, P. Sun and C. Duan, High resolution jet-cooled infrared absorption spectra of the formic acid dimer: A reinvestigation of the C-O stretch region, *J. Chem. Phys.*, 2014, **140**, 164311.
60 J. O. Richardson and S. C. Althorpe, Ring-polymer instanton method for calculating tunneling splittings, *J. Chem. Phys.*, 2011, **134**, 054109.
61 Y. Zhang, W. Li, W. Luo, Y. Zhu and C. Duan, High resolution jet-cooled infrared absorption spectra of $(HCOOH)_2$, $(HCOOD)_2$, and HCOOH–HCOOD complexes in 7.2 μm region, *J. Chem. Phys.*, 2017, **146**, 244306.
62 A. M. Santa Dara, G. Avila and E. Mátyus, Fingerprint region of the formic acid dimer: Variational vibrational computations in curvilinear coordinates, *Phys. Chem. Chem. Phys.*, 2021, **23**, 6526–6535.
63 W. Li, L. Evangelisti, Q. Gou, W. Caminati and R. Meyer, The barrier to proton transfer in the dimer of formic acid: A pure rotational study, *Angew. Chem., Int. Ed.*, 2019, **58**, 859–865.
64 O. T. Unke and M. Meuwly, PhysNet: A neural network for predicting energies, forces, dipole moments, and partial charges, *J. Chem. Theory Comput.*, 2019, **15**, 3678–3693.
65 U. Rivero, O. T. Unke, M. Meuwly and S. Willitsch, Reactive atomistic simulations of Diels–Alder reactions: The importance of molecular rotations, *J. Chem. Phys.*, 2019, **151**, 104301.
66 S. Brickel, A. K. Das, O. T. Unke, H. T. Turan and M. Meuwly, Reactive molecular dynamics for the [Cl–CH_3–Br]− reaction in the gas phase and in solution: a comparative study using empirical and neural network force fields, *Electron. Struct.*, 2019, **1**, 024002.
67 S. Käser, O. T. Unke and M. Meuwly, Isomerization and decomposition reactions of acetaldehyde relevant to atmospheric processes from dynamics simulations on neural network-based potential energy surfaces, *J. Chem. Phys.*, 2020, **152**, 214304.
68 B. C. Sweeny, H. Pan, A. Kassem, J. C. Sawyer, S. G. Ard, N. S. Shuman, A. A. Viggiano, S. Brickel, O. T. Unke and M. Upadhyay, *et al.*, Thermal activation of methane by MgO^+: Temperature dependent kinetics, reactive molecular dynamics simulations and statistical modeling, *Phys. Chem. Chem. Phys.*, 2020, **22**, 8913–8923.
69 J. Behler and M. Parrinello, Generalized neural-network representation of high-dimensional potential-energy surfaces, *Phys. Rev. Lett.*, 2007, **98**, 146401.
70 J. Gilmer, S. S. Schoenholz, P. F. Riley, O. Vinyals and G. E. Dahl, Neural message passing for quantum chemistry. Proc. of the 34th Int. Conf. on Machine Learning, vol. 70, 2017, pp. 1263–1272.
71 A. G. Baydin, B. A. Pearlmutter, A. A. Radul and J. M. Siskind, Automatic differentiation in machine learning: A survey, *J. Mach. Learn. Res.*, 2017, **18**, 5595–5637.
72 C. Møller and M. S. Plesset, Note on an approximation treatment for many-electron systems, *Phys. Rev.*, 1934, **46**, 618–622.
73 R. A. Kendall, T. H. Dunning Jr and R. J. Harrison, Electron affinities of the first-row atoms revisited. Systematic basis sets and wave functions, *J. Chem. Phys.*, 1992, **96**, 6796–6806.
74 H.-J. Werner, P. J. Knowles, G. Knizia, F. R. Manby, M. Schütz, P. Celani, W. Györffy, D. Kats, T. Korona, R. Lindh *et al.*, *MOLPRO, version 2019, a package of ab initio programs*, 2019.
75 A. H. Larsen, J. J. Mortensen, J. Blomqvist, I. E. Castelli, R. Christensen, M. Dułak, J. Friis, M. N. Groves, B. Hammer and C. Hargus, *et al.*, The atomic simulation environment – A Python library for working with atoms, *J. Phys.: Condens. Matter*, 2017, **29**, 273002.
76 J. J. P. Stewart, *S. C. C. MOPAC 2016*, Colorado Springs, CO, USA, 2016.
77 J. J. Stewart, Optimization of parameters for semiempirical methods V: modification of NDDO approximations and application to 70 elements, *J. Mol. Model.*, 2007, **13**, 1173–1213.
78 G. M. Torrie and J. P. Valleau, Nonphysical sampling distributions in Monte Carlo free-energy estimation: Umbrella sampling, *J. Comput. Phys.*, 1977, **23**, 187–199.
79 B. Huang and O. A. von Lilienfeld, Quantum machine learning using atom-in-molecule-based fragments selected on the fly, *Nat. Chem.*, 2020, **12**, 945–951.
80 J. Behler, Perspective: Machine learning potentials for atomistic simulations, *J. Chem. Phys.*, 2016, **145**, 170901.
81 J. Behler, Constructing high-dimensional neural network potentials: A tutorial review, *Int. J. Quantum Chem.*, 2015, **115**, 1032–1050.
82 J. S. Smith, O. Isayev and A. E. Roitberg, ANI-1, A data set of 20 million calculated off-equilibrium conformations for organic molecules, *Sci. Data*, 2017, **4**, 170193.
83 J. A. Pople, M. Head-Gordon and K. Raghavachari, Quadratic configuration interaction. A general technique for determining electron correlation energies, *J. Chem. Phys.*, 1987, **87**, 5968–5975.

Open Access Article. Published on 26 October 2021. Downloaded on 2/16/2026 3:25:57 PM. This article is licensed under a Creative Commons Attribution-NonCommercial 3.0 Unported Licence.

84 G. D. Purvis III and R. J. Bartlett, A full coupled-cluster singles and doubles model: The inclusion of disconnected triples, *J. Chem. Phys.*, 1982, **76**, 1910–1918.
85 M. Thomas, M. Brehm, R. Fligg, P. Vöhringer and B. Kirchner, Computing vibrational spectra from ab initio molecular dynamics, *Phys. Chem. Chem. Phys.*, 2013, **15**, 6608–6622.
86 M. Schmitz and P. Tavan, Vibrational spectra from atomic fluctuations in dynamics simulations. I. Theory, limitations, and a sample application, *J. Chem. Phys.*, 2004, **121**, 12233–12246.
87 M. Schmitz and P. Tavan, Vibrational spectra from atomic fluctuations in dynamics simulations. II. Solvent-induced frequency fluctuations at femtosecond time resolution, *J. Chem. Phys.*, 2004, **121**, 12247–12258.
88 V. Barone, Anharmonic vibrational properties by a fully automated second-order perturbative approach, *J. Chem. Phys.*, 2005, **122**, 014108.
89 J. B. Anderson, A random-walk simulation of the Schrödinger equation: H_3^+, *J. Chem. Phys.*, 1975, **63**, 1499–1503.
90 I. Kosztin, B. Faber and K. Schulten, Introduction to the diffusion Monte Carlo method, *Am. J. Phys.*, 1996, **64**, 633–644.
91 M. Abadi, P. Barham, J. Chen, Z. Chen, A. Davis, J. Dean, M. Devin, S. Ghemawat, G. Irving, M. Isard, *et al.*, Tensorflow: A system for large-scale machine learning. 12th USENIX symposium on operating systems Design and Implementation (OSDI 16), 2016, pp. 265–283.
92 R. J. DiRisio, F. Lu and A. B. McCoy, GPU-accelerated neural network potential energy surfaces for diffusion Monte Carlo, *J. Phys. Chem. A*, 2021, **125**, 5849–5859.
93 Z. Xue, *Raman spectroscopy of carboxylic acid and water aggregates*, Logos Verlag Berlin GmbH, 2011.
94 F. Kollipost, Dissertation: Schwingungsdynamik in O–H···O-verbrückten Aggregaten: FTIR-Spektroskopie vom Nah- bis zum Ferninfraroten, 2015, http://hdl.handle.net/11858/00-1735-0000-0023-9644-9.
95 J. E. Bertie and K. H. Michaelian, The Raman spectra of gaseous formic acid-h_2 and-d_2, *J. Chem. Phys.*, 1982, **76**, 886–894.
96 K. A. Meyer and M. A. Suhm, Vibrational exciton coupling in homo and hetero dimers of carboxylic acids studied by linear infrared and Raman jet spectroscopy, *J. Chem. Phys.*, 2018, **149**, 104307.
97 F. Kollipost, R. W. Larsen, A. Domanskaya, M. Nörenberg and M. Suhm, Communication: The highest frequency hydrogen bond vibration and an experimental value for the dissociation energy of formic acid dimer, *J. Chem. Phys.*, 2012, **136**, 151101.
98 P. R. Franke, J. F. Stanton and G. E. Douberly, How to VPT2: accurate and intuitive simulations of CH stretching infrared spectra using VPT2 + K with large effective Hamiltonian resonance treatments, *J. Phys. Chem. A*, 2021, **125**, 1301–1324.
99 V. Barone, M. Biczysko, J. Bloino, M. Borkowska-Panek, I. Carnimeo and P. Panek, Toward anharmonic computations of vibrational spectra for large molecular systems, *Int. J. Quantum Chem.*, 2012, **112**, 2185–2200.
100 Z.-H. Xu and M. Meuwly, Vibrational spectroscopy and proton transfer dynamics in protonated oxalate, *J. Phys. Chem. A*, 2017, **121**, 5389–5398.
101 T. Häber, U. Schmitt, C. Emmeluth and M. A. Suhm, Ragout-jet FTIR spectroscopy of cluster isomerism and cluster dynamics: from carboxylic acid dimers to N_2O nanoparticles, *Faraday Discuss.*, 2001, **118**, 331–359.
102 Y. T. Chang, Y. Yamaguchi, W. H. Miller and H. F. Schaefer III, An analysis of the infrared and Raman spectra of the formic acid dimer $(HCOOH)_2$, *J. Am. Chem. Soc.*, 1987, **109**, 7245–7253.
103 J. E. Bertie, K. H. Michaelian, H. H. Eysel and D. Hager, The Raman-active O–H and O–D stretching vibrations and Raman spectra of gaseous formic acid-d_1 and -OD, *J. Chem. Phys.*, 1986, **85**, 4779–4789.
104 I. Yokoyama, Y. Miwa and K. Machida, Extended molecular mechanics calculations of thermodynamic quantities, structures, vibrational frequencies, and infrared absorption intensities of formic acid monomer and dimer, *J. Am. Chem. Soc.*, 1991, **113**, 6458–6464.
105 Y. Maréchal, IR spectra of carboxylic acids in the gas phase: A quantitative reinvestigation, *J. Chem. Phys.*, 1987, **87**, 6344–6353.
106 D. Berckmans, H. P. Figeys, Y. Marechal and P. Geerlings, *Ab initio* and LMO studies on the integrated intensities of infrared absorption bands of polyatomic molecules. 7. The formic acid dimer. Influence of hydrogen bonding and isotopic substitution, *J. Phys. Chem.*, 1988, **92**, 66–73.
107 J. Toulouse, R. Assaraf and C. J. Umrigar *Advances in Quantum Chemistry*, Elsevier, 2016, vol. 73, pp. 285–314.
108 M. Suhm and F. Kollipost, Femtosecond single-mole infrared spectroscopy of molecular clusters, *Phys. Chem. Chem. Phys.*, 2013, **15**, 10702–10721.
109 S. Lammers, S. Lutz and M. Meuwly, Reactive force fields for proton transfer dynamics, *J. Comput. Chem.*, 2008, **29**, 1048–1063.
110 P. Houston, R. Conte, C. Qu and J. M. Bowman, Permutationally invariant polynomial potential energy surfaces for tropolone and H and D atom tunneling dynamics, *J. Chem. Phys.*, 2020, **153**, 024107.
111 D. Koner and M. Meuwly, Permutationally invariant, reproducing kernel-based potential energy surfaces for polyatomic molecules: From formaldehyde to acetone, *J. Chem. Theory Comput.*, 2020, **16**, 5474–5484.
112 Y.-J. Zhang, A. Khorshidi, G. Kastlunger and A. A. Peterson, The potential for machine learning in hybrid QM/MM calculations, *J. Chem. Phys.*, 2018, **148**, 241740.
113 P. M. Felker, Y. Liu, J. Li and Z. Bacic, DCl–H_2O, HCl–D_2O, and DCl–D_2O dimers: Inter-and intramolecular vibrational states and frequency shifts from fully coupled quantum calculations on a full-dimensional neural network potential energy surface, *J. Phys. Chem. A*, 2021, **125**, 6437–6449.
114 J. Zeng, L. Cao, M. Xu, T. Zhu and J. Z. Zhang, Complex reaction processes in combustion unraveled by neural network-based molecular dynamics simulation, *Nat. Commun.*, 2020, **11**, 1–9.